BNL-108183-2015-JA

Mon. Not. R. Astron. Soc. **000**, 1–18 (0000) Printed 19 February 2015 (MN LaTeX style file v2.2)

The LMC geometry and outer stellar populations from early DES data

Eduardo Balbinot[1,2,3⋆], B. X. Santiago[2,3], L. Girardi[4], A. Pieres[2,3], L. N. da Costa[3,5], M. A. G. Maia[3,5], R. A. Gruendl[6,7] A. R. Walker[8], B. Yanny[9], A. Drlica-Wagner[9], A. Benoit-Levy[10], T. M. C. Abbott[8], S. S. Allam[9,11], J. Annis[9], J. P. Bernstein[12], R. A. Bernstein[13], E. Bertin[14], D. Brooks[10], E. Buckley-Geer[9], A. Carnero Rosell[3,5], C. E. Cunha[15], D. L. DePoy[16], S. Desai[17,18], H. T. Diehl[9], P. Doel[10], J. Estrada[9], A. E. Evrard[19,20,14], A. Fausti Neto[3], D. A. Finley[9], B. Flaugher[9], J. A. Frieman[9,18], D. Gruen[17,21], K. Honscheid[22], D. James[8], K. Kuehn[23], N. Kuropatkin[9], O. Lahav[10], M. March[24], J. L. Marshall[16], C. Miller[19,20], R. Miquel[25,26] R. Ogando[3,5], J. Peoples[9], A. Plazas[27], V. Scarpine[9], M. Schubnell[12], I. Sevilla-Noarbe[28], R. C. Smith[8], M. Soares-Santos[9], E. Suchyta[22], M. E. C. Swanson[7], G. Tarle[19], D. L. Tucker[9], R. Wechsler[29,18], J. Zuntz[30]
(Affiliations can be found after the references)

19 February 2015

ABSTRACT
The Dark Energy Camera has captured a large set of images as part of Science Verification (SV) for the Dark Energy Survey. The SV footprint covers a large portion of the outer Large Magellanic Cloud (LMC), providing photometry 1.5 magnitudes fainter than the main sequence turn-off of the oldest LMC stellar population. We derive geometrical and structural parameters for various stellar populations in the LMC disk. For the distribution of all LMC stars, we find an inclination of $i = -38.14° \pm 0.08°$ (near side in the North) and a position angle for the line of nodes of $\theta_0 = 129.51° \pm 0.17°$. We find that stars younger than ~ 4 Gyr are more centrally concentrated than older stars. Fitting a projected exponential disk shows that the scale radius of the old populations is $R_{>4Gyr} = 1.41 \pm 0.01$ kpc, while the younger population has $R_{<4Gyr} = 0.72 \pm 0.01$ kpc. However, the spatial distribution of the younger population deviates significantly from the projected exponential disk model. The distribution of old stars suggests a large truncation radius of $R_t = 13.5 \pm 0.8$ kpc. If this truncation is dominated by the tidal field of the Galaxy, we find that the LMC is $\simeq 24^{+9}_{-6}$ times less massive than the encircled Galactic mass. By measuring the Red Clump peak magnitude and comparing with the best-fit LMC disk model, we find that the LMC disk is warped and thicker in the outer regions north of the LMC centre. Our findings may either be interpreted as a warped and flared disk in the LMC outskirts, or as evidence of a spheroidal halo component.

Key words: galaxies: Magellanic Clouds; galaxies: stellar content; stars: statistics

1 INTRODUCTION

The Milky Way (MW) satellite system offers a variety of examples of dwarf galaxies. Most of its members are essentially gas-free and contain mainly old stars (McConnachie 2012). The evolution of these systems is closely related to the formation of the Galaxy and the process of mass assembly of the large scale structures in the Universe (Klypin et al. 1999; Moore et al. 1999; Stewart et al. 2008). On the other hand, the Large and Small Magellanic Clouds (LMC and SMC,

⋆ e-mail: e.balbinot@surrey.ac.uk

© 0000 RAS

respectively) are the closest low-mass, gas-rich (Grcevich & Putman 2009) interacting systems. The main features tracing the interaction history of the clouds are the HI Magellanic Stream (Mathewson, Cleary & Murray 1974), and Bridge (Hindman, Kerr & McGee 1963). A counterpart of the Stream was found and named the Leading Arm (Putman et al. 1998). The formation of these structures is a subject of great debate. Recent simulations favour a scenario where the Stream, Bridge, and Leading Arm are remains from the close interaction between the LMC and SMC before falling into the MW potential (Besla et al. 2012; Kallivayalil et al. 2013).

The Clouds' star formation history (SFH) also reflects their close interaction history. It is possible to identify multiple periods of enhanced star formation that are arguably correlated with close encounter between the Clouds (Meschin et al. 2014; Rubele et al. 2012; Javiel, Santiago & Kerber 2005; Holtzman et al. 1999). Evidence of such events are imprinted in the stellar population which, due to the proximity of the Magellanic System, is resolved into individual stars with medium sized ground-based telescopes. Enhanced star formation is also demonstrated by the extensive star cluster system throughout the Magellanic Clouds (MC). The clusters in this system span a very broad range in age and metallicity (Kerber & Santiago 2009). Evidence of an age-gap (Jensen, Mould & Reid 1988) may support a relationship between the formation/disruption rate of star clusters and the intergalactic interaction history. In this sense the star clusters in the LMC may give hints to how the intergalactic interaction affects the evolution of star cluster systems (Renaud & Gieles 2013).

Despite being the nearest interacting system of galaxies, the Magellanic System still has only a small angular fraction observed to the photometric depth of its old main sequence turn-off (MSTO). Deep observations suggest that the LMC stellar populations extend beyond an angular distance of 15° from its centre (Majewski et al. 2009). There is also kinematic evidence for a dynamically warm stellar component consistent with a halo (Minniti et al. 2003) that has its major axis oriented with the disk (Alves 2004).

Very few studies are available in the outskirts of the LMC. Weinberg & Nikolaev (2001) report an exponential scale length of $R_s \sim 1.4$ kpc with no significant distinction between a young and old disk; however, their sample is from the 2 Micron All-Sky Survey (2MASS; Skrutskie et al. 2006), which is very shallow and does not allow for a clear age selection. Saha et al. (2010) report a smaller scale length of $R_s = 1.15$ kpc based on an optical survey. They argue in favour of a truncation radius of $R_t \sim 14$ kpc. Their sample is limited to only a few fields and their analysis does not use age selected stellar samples.

A new generation of photometric surveys is now coming to the Southern Hemisphere, allowing for the first time a complete view of the Magellanic System. One of them is the Dark Energy Survey (DES), which will observe the outskirts of the LMC, SMC, and most of the Magellanic Stream over the course of 5 years. DES is a photometric survey with the primary goal of measuring the dark energy equation of state. To achieve this goal the survey will employ four independent cosmological probes: galaxy clusters, baryon acoustic oscillations, weak lensing, and type Ia supernovae (Flaugher 2005). The total survey area is ~ 5000 deg^2 reaching a magnitude limit of $i \sim 24$. The photometric system adopted for DES comprises the filters g, r, i, z, which are similar to the ones used in the Sloan Digital Sky Survey (SDSS; Fukugita et al. 1996), with the addition of the Y passband, which provides synergy with the VISTA Hemisphere Survey (McMahon 2012; Cioni et al. 2011). The DES footprint will overlap with several other surveys in the southern hemisphere allowing a multi wavelength approach to various astrophysical problems.

An early release of DES Science Verification (SV) data was made available to the DES collaboration recently. The data cover ∼200 deg^2 of the southern sky and sample regions as close as 4° North from the LMC centre. The photometric catalogue from this release reaches ~ 1.5 mag fainter than the old MSTO of the LMC (which is at $g \sim 22$), allowing for a detailed study of the resolved stellar population of this galaxy.

In this paper we use the DES SV data to study the LMC geometry and density profile as traced by stellar components with a characteristic age range. We model the distribution of stars using a simple projected exponential disk and perform a formal fit. We discuss the presence of a possible truncation radius and its implication for the LMC mass. As an alternative probe of the LMC geometry we use Red Clump (RC) stars as a distance indicator and a ruler for the LMC thickness. This paper is organized as follows. In Section 2 we present a brief introduction to the DES SV data. In Section 3 we discuss the quality of the photometry and address issues due to completeness and survey coverage. In Section 4 we describe the disk model and the fitting procedure used to find the geometrical parameters of the LMC. Section 5 shows our efforts to use the RC as a distance and thickness estimator. In Section 6 we summarize and discuss the implications of the results found in this paper.

2 DECAM AND DES SCIENCE VERIFICATION

The Dark Energy Camera (DECam) (Flaugher et al. 2010) was constructed in order to carry out the Dark Energy Survey. This instrument has a focal plane comprised of 74 CCDs: 62 2k×4k CCDs dedicated to science imaging and 12 2k×2k CCDs for guiding, focus, and alignment. The camera is also equipped with a five element optical corrector and a sophisticated cryogenic cooling system. DECam is installed at the prime focus of the Cerro Tololo Inter-American Observatory (CTIO) 4 meter Blanco telescope. In this configuration, DECam has a 2.2 degree-wide field-of-view (FoV) and a central pixel scale of 0.263 ″/px. In typical site conditions, the Blanco telescope plus DECam yield an imaging point spread function (PSF) with full-width half maximum (FWHM) of 0.9″, which is adequately sampled by the pixel scale.

DECam was commissioned in September 2012 and began operations in November 2012, with the DES SV campaign covering a period of three months. The DES SV data is intended to test capabilities of the camera, the data transfer infrastructure, and the data processing. All images taken during SV are public; however, the catalogues generated by the collaboration are proprietary.

2.1 Data reduction

The DES data management (DESDM) team was responsible for the reduction of the SV images. Here we will give a brief description of the reduction process. For a complete description we refer to Sevilla et al. (2011), Desai et al. (2012), and Mohr et al. (2012).

The DESDM data reduction pipeline consists of the following steps:

Image detrending: this step includes correction for crosstalk between CCD amplifier electronics, bias level correction, correction for pixel-to-pixel sensitivity variation (flat-fielding), as well as corrections for non-linearity, fringing, pupil, and illumination.

Astrometric calibration: in this step, bright known stars are identified in a given image using SExtractor (Bertin & Arnouts 1996). The position of these stars in the focal plane is used to find the astrometric solution with the aid of the software SCAMP (Bertin 2006) through comparison to UCAC-4 (Zacharias et al. 2013).

Nightly photometric calibration: several reference stars are observed each night, and a photometric equation is derived for that night. This equation takes into account a zero point, a colour term, and an airmass term for each of the DECam science CCDs.

Global calibration: relative photometric calibration of the DES survey area is done with repeated observations of the same star in overlapping DECam exposures using a method similar to that described in Glazebrook et al. (1994). The relative magnitudes are anchored to a small set of absolutely calibrated reference stars within the same area called tertiary standards which come from observations on photometric nights. They are then calibrated relative to known equatorial belt standards observed on the same night with the same filter set (Tucker et al. 2007). The current accuracy of the relative and absolute systems is a few percent, and is expected to improve as the DES survey covers larger contiguous areas. DES calibration was checked using the Star Locus Regression technique (Kelly et al. 2014). This analysis revealed that zero-point offsets are typically less than 0.05 mag in g, r, i, and z across the DES footprint observed so far.

Coaddition: in order to increase the signal-to-noise ratio, exposures are combined. This has the advantage of mitigating transient objects, such as cosmic rays and satellite trails. This step requires the placement of the images in a common reference projection. The software SWarp (Bertin et al. 2002) was used and the coaddition process was done in segments of the sky called *tiles*. At this stage the flux is corrected according to the photometric calibration described above.

Cataloging: for each coadded *tile* source detection and model-fitting photometry is performed using PSFEx and SExtractor (Bertin 2011; Bertin & Arnouts 1996) on a combined r, i, and z image. Object fluxes and many other characteristics are calculated in the individual g, r, i, z, Y frames. These catalogues are ingested into a high performance database system.

The final catalogue is available for the DES collaboration through a database query client. There are approximately 900 parameters measured for each source identified by SExtractor. In Table 1 we list a few parameters relevant to this work. In the same table we also list any comments about the parameter and the quality cuts applied.

Table 1. Here we show a subset of the SExtractor parameters measured for the coadded DECam SV data. We also show any selection criteria that were made.

Parameter name	Selection
`RA`	–
`DEC`	–
`MAG_AUTO_*`	$\leqslant 26.0$ in g and r
`MAGERR_AUTO_*`	–
`SPREAD_MODEL_*`	$\lvert$`SPREAD_MODEL_I`$\rvert \leqslant 0.002$
`FLAGS_*`	$\leqslant 3$ in g and r

The $*$ symbol refers to all passbands available.

3 THE SV DATA

By the end of the SV campaign, DECam had obtained images in five passbands of a region with roughly 300 deg^2, for which 200 deg^2 are contiguous. The contiguous region covers the northern outskirts of the LMC. This region overlaps an eastern portion of the South Pole Telescope (SPT) footprint (Carlstrom et al. 2011). Hence we call it SPT-E for simplicity.

In this section we will discuss several aspects of the SV data and how it is suitable for the analysis we propose.

3.1 Photometry

Currently, the deepest and most homogeneous magnitude measurement resulting from the DESDM pipeline is `MAG_AUTO`, which is computed using the flux inside a Kron radius (Kron 1980). The Kron radius is dependent on how extended a source is, hence the aperture is variable, but it is essentially the same for all stars, given that there are no significant spatial dependence in the image quality, which is the case for DES observations. Thus, `MAG_AUTO` is roughly equivalent to a simple aperture magnitude but less sensitive to seeing variations. We adopt the following notation throughout the paper: g is the `MAG_AUTO` magnitude measured for the g passband. This also applies for the magnitudes measured in r, i, z, Y.

The raw DESDM catalogue has approximately 10^8 sources with $g \leqslant 24.6$. This list includes spurious detections like satellite trails, star wings, cosmic rays, etc. To exclude such detections from our catalogue we adopt a simple cut in the `FLAGS` parameter. We select only sources that simultaneously have `FLAGS_G` and `FLAGS_R` $\leqslant 3$, which selects objects that are not saturated and do not contain any bad pixel. The `FLAGS` code is the same as the one adopted by SExtractor. The number of sources left after this cut is $\sim 9 \times 10^7$.

We check the stability of the photometric calibration provided by DESDM by comparing the RC peak colour at different points of the SPT-E that contain LMC stars. For all bands we found a maximum scatter of 0.02 mags around the RC peak colour.

Table 2. Some general photometric system information: the central wavelength (λ_c) in nanometres, the extinction as a fraction of the extinction in the Johnson V passband (assuming $R_V = 3.1$ and a Cardelli, Clayton & Mathis (1989) extinction curve for the MW), and the value of the magnitude corresponding to a typical signal-to-noise ratio of 10. In the last three columns the coefficients of the best-fit error model are shown.

Filter	λ_c (nm)	A_λ/A_V	$m_{10\%}$	(a, b, c)
g	479	1.199	23.94	(0.001, 26.41, 1.25)
r	641	0.837	23.76	(0.001, 26.34, 1.27)
i	781	0.635	22.75	(0.003, 25.52, 1.34)
z	924	0.462	22.03	(0.003, 24.75, 1.43)
Y	1008	0.400	20.50	(0.009, 23.45, 1.40)

The following model was adopted to describe the photometric uncertainties from the DECam SV data.

$$\sigma(mag) = a + \exp\left(\frac{mag - b}{c}\right) \quad (1)$$

By fitting the above equation to a sample of 0.01% randomly chosen stars from the SPT-E region we find the error curves shown in Figure 1. The coefficients for each curve are given on Table 2, where we also show the 10% uncertainty magnitude for each band. Along with these values we also give some basic information about the filter central wavelength and extinction coefficients at those wavelengths from Cardelli, Clayton & Mathis (1989).

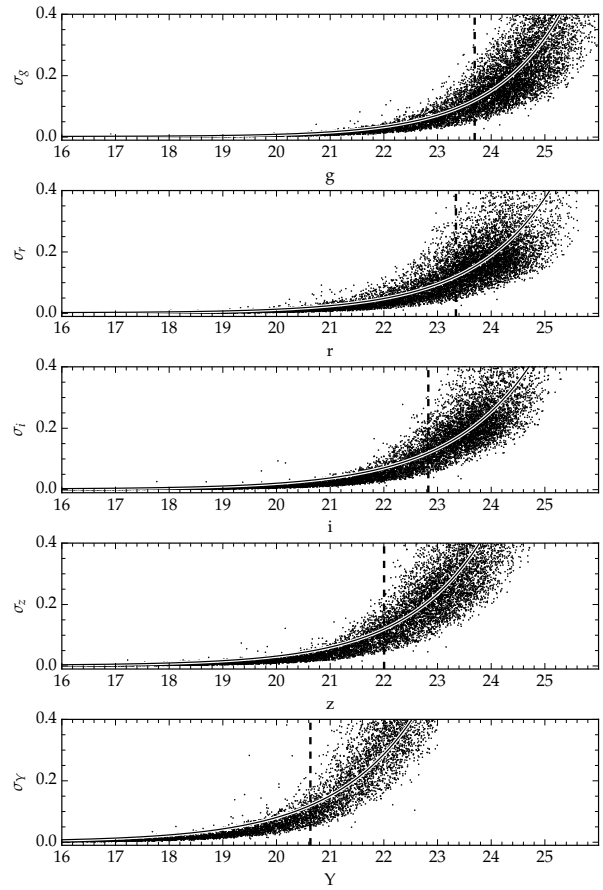

Figure 1. Magnitude versus uncertainty for a sample of 0.01% of the total number of stars in the DECam SV region. The solid curve shows the best-fit error model. The coefficients are given in Table 2. The dashed line shows the 10% uncertainty magnitude.

3.2 Star/Galaxy Separation

The DES collaboration has generated several datasets for validating and testing the DESDM system (Mohr et al. 2012). These datasets were simulations of the actual observations. To create these *mock* observations, input catalogues of artificial galaxies and stars were generated (Rossetto et al. 2011; Balbinot et al. 2012; Busha 2014). The mock observations included a time varying seeing, realistic shapes for the galaxies, and variations to the focal plane of DECam. These images were fed into the DESDM reduction pipeline and an output catalogue was generated, which was then released to the collaboration to perform tests of their scientific algorithms.

Tests with a set of such simulations, called Data Challenge 5 (DC5) by the collaboration, have been carried out in order to assess how different star-galaxy classification parameters perform. A summary of this comparison is shown in Rossetto et al. (2011). The main conclusion is that `SPREAD_MODEL` (Desai et al. 2012; Bouy et al. 2013) performs better in terms of purity and completeness than other typically employed classifiers such as `CLASS_STAR` and `FLUX_RADIUS` (Bertin & Arnouts 1996). Later, Soumagnac et al. (2013) developed a more sophisticated star-galaxy separation algorithm; however, this algorithm must be trained on a data set where true stars and galaxies are known. Implementation of such methods are being considered collaboration wide. For simplicity, we choose to use `SPREAD_MODEL` measured in the i band as the star-galaxy separator. The cut-off criterion for selecting stars is $|\texttt{SPREAD_MODEL_I}| \leqslant 0.002$. From test on DC5, this cut is found to correspond to a simultaneous stellar completeness and purity of $\simeq 80\%$ for objects with $g < 23$ (Rossetto et al. 2011). From this point further we call objects that match this cut-off criteria *stars*. It is worth mentioning that at $g = 23$ we expect $\sim 20\%$ of contamination from galaxies in our sample. However, the large scale distribution of these objects is homogeneous and is unlikely to significantly affect the findings of this paper.

3.3 Completeness

To independently assess the completeness of the DESDM catalog we conducted a few experiments using DAOPHOT (Stetson 1987). This photometry code is known to perform very well in extremely crowded regions such as the cores of globular clusters (Balbinot et al. 2009). Hence, at the typical density of LMC field stars it should yield a fairly complete catalogue. This DAOPHOT catalogue may be compared to the one produced by DESDM as an approximation to a complete catalogue and giving an estimate of the completeness as function of magnitude. This is not the most accurate approach to this problem; however, it is much simpler than performing artificial star experiments across several hundred squared degrees.

We performed DAOPHOT photometry on 51 fields, 50 of which contained a LMC star cluster in its centre. The $51^{\rm st}$ field was selected as far away as available in the SPT-E

data in order to sample a region where there are few or no LMC stars. The fields selected are subregions of the coadded images encompassing $6.75' \times 6.75'$ each, with the exception of the 51st field, which has $18' \times 36'$. The first 50 fields were selected in order to assess the completeness not only in regions with a density of stars typical of the LMC, but also with varying density, such as the inner regions of a star cluster. A broader discussion about this subject will be presented in a future paper. The 51st field was selected in order to compare the performance of the DESDM reduction pipeline in a region with little or no crowding. The position of each of the all 51 fields is marked on Figure 2. On average DESDM and DAOPHOT photometry agree within 0.02 in g and r.

To compare the number of stars as a function of magnitude, we cut both the DESDM and DAOPHOT catalogues at the 3% photometric uncertainty level. This cut happens at $g \simeq 23.5$. To separate stars from galaxies in DAOPHOT we adopted a cut in the *sharpness* parameter which behaves similarly to `SPREAD_MODEL`.

In Figure 3 top panel we show the ratio between the number of stars detected by DESDM and DAOPHOT ($N_{DES}/N_{DAOPHOT}$) averaged in magnitude bins for the 51 fields discussed above. The solid line shows the average value at a given magnitude bin. The shaded region shows the standard deviation. In the two bottom panels in the same figure we show the value of $N_{DES}/N_{DAOPHOT}$ as a function of angular separation to the LMC centre. We show this for two magnitude bins: $21.8 < g \leqslant 22.6$ and $22.6 < g \leqslant 23.3$ (also indicated in the figure). From Figure 3 we notice that the average completeness drops as a function of increasing magnitude, as expected. The completeness remains roughly constant as a function of angular separation to the LMC centre with a spread of the same order as the one shown in the shaded region of the top panel. We conclude that the completeness has little spatial dependence at least up to magnitudes as faint as $g \sim 23$.

Despite the good performance in moderately crowded fields (i.e. LMC field population), we observed that in the inner regions of star clusters the DESDM sample is highly incomplete reaching less than 40% completeness for $g = 19$ and dropping to zero for fainter magnitudes. This will be further explored in future publications.

We note that where the completeness is most important to our results regarding truncation radii and scale lengths, i.e. at distances farther away from the center of the LMC, the star density is low enough that crowding effects do not affect the sample selection as shown in Figure 3.

From the completeness analysis described above we conclude that in the DESDM catalogue completeness does not depend strongly on source density, except in extremely crowded environments such as the central parts of stars clusters. From visual inspection and through comparison with state-of-the-art crowded field photometry methods we find no strong evidence for large-scale variations in the stellar completeness in the SPT-E region, thus allowing us to properly access the spatial distribution of stars across its footprint, either from the LMC or from the MW.

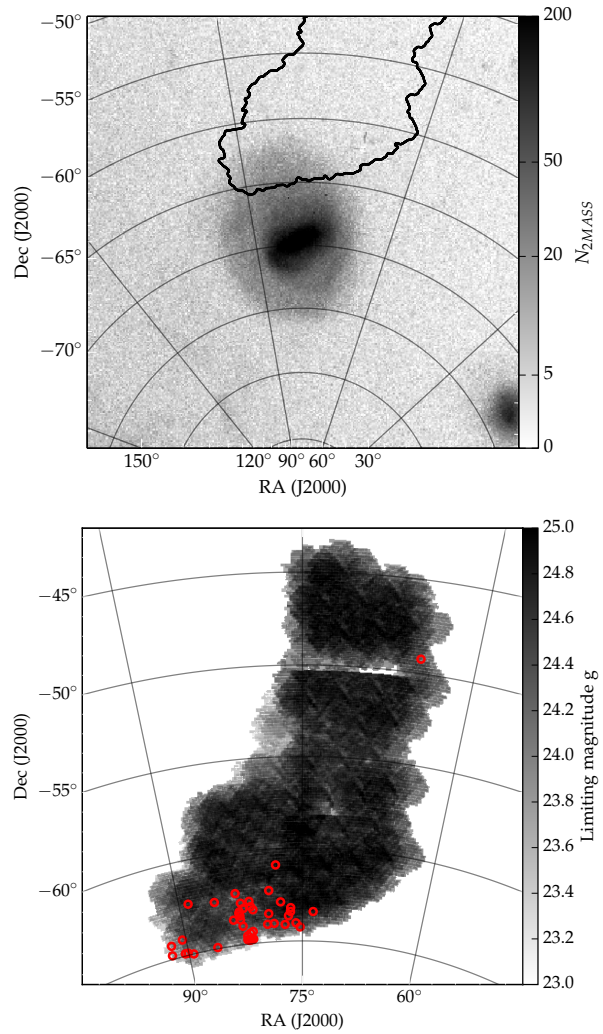

Figure 2. Top panel: Gnomonic projection of the number of 2MASS stars that are consistent with AGB and RGB stars according to Yang et al. (2007). The projection is centred in the LMC centre. Part of the SMC is visible in the lower right corner. The solid contour shows an approximate footprint of the southern part of the SPT-E region of the DES SV data. Bottom panel: Gnomonic projection of a N_{side}=4096 HEALPIX map of the g magnitude limit MANGLE mask for the SPT-E region quoted above. Holes and unobserved regions are masked and shown in white. Red circles mark the position of the fields selected for assessing the survey completeness.

3.4 Mangle masks

We use the MANGLE software (Swanson et al. 2008) to track the survey coverage and limiting magnitude. Along with the release of the DESDM catalogues, a set of MANGLE masks was also provided. These masks contain information about the limiting magnitude in each patch of the sky, as well as other key information about data quality. The magnitude limit is computed as the detection limit of a point source with signal-to-noise ratio $S/N = 10$. The noise is estimated from the variance and level of the sky on a patch of the sky. To measure the flux an aperture of $1''$ radius is used; this yields a magnitude measurement called `MAG_APER_4`. For a

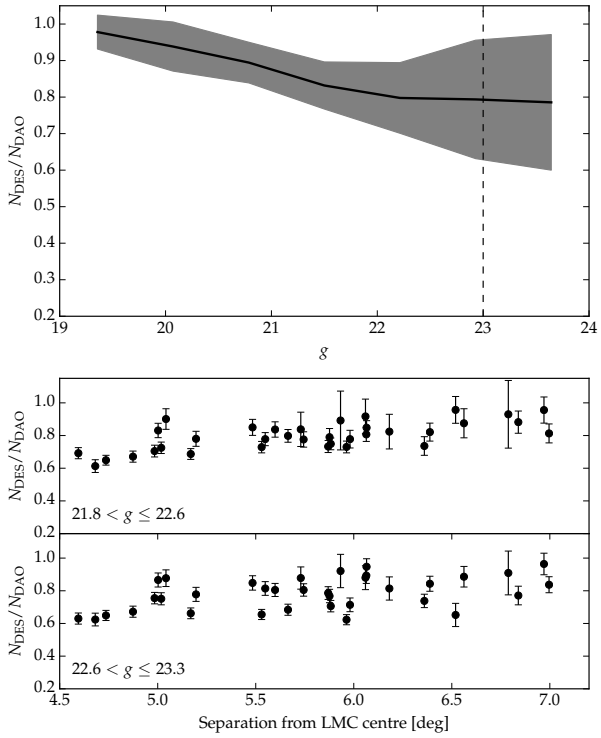

Figure 3. *Top panel:* we show the ratio of stars detected by DESDM and DAOPHOT as a function of g magnitude. The solid line shows the average for the 51 fields analysed. The shaded region shows the standard deviation for the 51 fields. The dashed vertical line shows the faintest magnitude limit used in this work. *Bottom panels:* black circles show the same ratio as in the top panel but now as a function of angular separation to the LMC centre for two magnitude bins (indicated in the captions). The error bars are computed using the Poisson uncertainty.

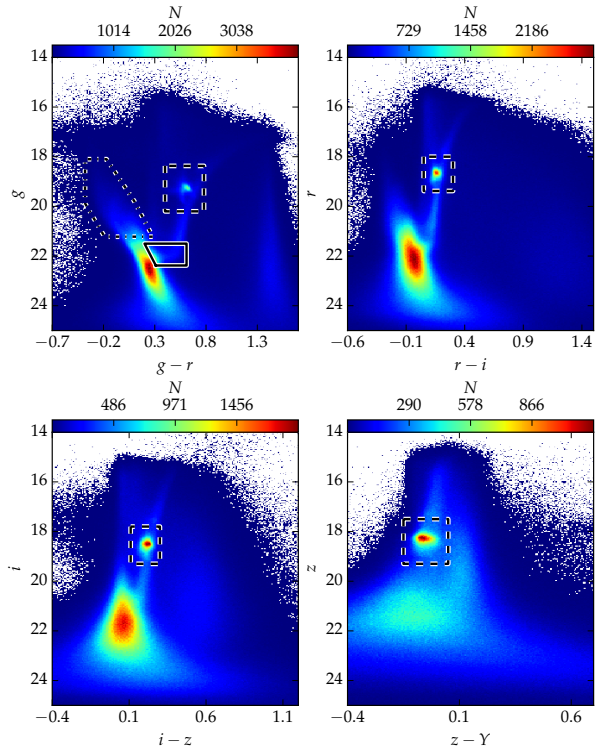

Figure 4. The Hess diagrams in each set of colour and magnitude available in the DES photometric system. In the top left panel we also show the colour-magnitude polygons used to select stars consistent with a young/intermediate (dot dashed polygon) and old (solid polygon) stellar population. The boxes (dashed) used for the selection of RC stars are shown in all panels.

complete description of the masks we refer to Swanson et al. (2012).

In Figure 2 we show the number of AGB and RGB stars found in 2MASS according to Yang et al. (2007) with the southern limits of the SPT-E region overplotted (top panel). We also show an approximation of the magnitude limit Mangle mask for the SPT-E region (bottom panel). It is an approximation in the sense that it uses the value of the Mangle mask at the central position of each pixel in the sky. The gray scale represents the magnitude limit at each point of the footprint. Holes caused by bright stars or other image imperfections are displayed as well. These regions have a magnitude limit of zero, hence going out of the gray scale range. The white color in the figure represents regions that were not observed. The figure uses a HEALpix pixelization (Górski et al. 2005) with N_{side}=4096 and a Gnomonic projection centered at $(\alpha, \delta) = (75°, -55°)$.

The approximate mask discussed above allows us to deal with the full SPT-E mask in a much faster way and at the same time to provide a very good approximation of the general properties of the survey, such as coverage and magnitude limits. The coverage mask is simply a HEALpix map with the value of 1 for pixels that were observed and 0 for those that were not or were masked for some reason. The coverage mask originally did not contain holes due to star clusters. To mask these regions we conducted a visual search for star clusters in the SPT-E and used the position of each cluster to add a hole in the mask (i.e. a region with coverage equals to zero).

The approximated masks were used to remove stars residing in regions where the following criteria were met: (i) a limiting g or r magnitude brighter than 23; (ii) coverage value equal to 0. The additional trimming for zero mask values was necessary because the original catalogue was limited by the *exact* masks, not the approximated ones.

The above section outlines the process of trimming the catalogue to select objects that are likely stars and to keep only regions with deep photometry that were not affected by artifacts in the survey. This catalogue, as well as the mask associated with it, will be used in the remainder of this paper.

4 THE LMC GEOMETRY

Classically, the LMC is classified as an Irregular Dwarf Galaxy, although it has several major components of a spiral galaxy such as a disk and a bar. It is, perhaps, more appropriate to classify this galaxy as a highly perturbed spiral galaxy. Its morphology departs so much from a classical Irregular Dwarf that it has been established that the LMC is the prototype of a class of dwarf galaxies called Magellanic Irregular (de Vaucouleurs & Freeman 1972). These galaxies

are characterized by being gas-rich, one-armed spirals with off-centre bars.

The SMC is the closest neighbour to the LMC. Together they form the Magellanic System. Recent dynamical modelling (Besla et al. 2012) and high precision tangential velocity measurements (Kallivayalil et al. 2013) point to the need for updated thinking with regard to the origins of the Magellanic System. The centre of mass spatial velocity of these galaxies is very close to the escape velocity of the MW, thus suggesting that the system is not gravitationally bound to the MW. The same models also predict the formation of the Magellanic Bridge and Stream as a result of the interaction of the LMC with the SMC, generating long arms of debris in the same fashion as the Antennae system.

Despite the growing number of simulations and high precision velocity measurements, a few aspects of the LMC geometry, such as the presence of a spheroidal halo (Majewski et al. 2009), and the warping and flaring of the disk (Subramaniam & Subramanian 2009) remain uncertain to some degree. New large area surveys in the Southern Hemisphere are beginning to shed light on these uncertainties.

Here we study the LMC disk geometry using a very simple approach. We try to model its stellar density using a circular exponential disk. This disk is inclined relative to the sky plane by the angle i. To compute the expected number of stars ρ as a function of α and δ we use the transformations found in Weinberg & Nikolaev (2001). For the sake of clarity, we give the expression for the heliocentric distance t to a given point of the disk with coordinates (α, δ).

$$\begin{aligned} t(\alpha,\delta) = -R_{LMC}\cos i \times \{&\cos\delta\sin(\alpha-\alpha_0)\sin\theta\sin i \\ &+ [\sin\delta\cos\delta_0 - \cos\delta\sin\delta_0\cos(\alpha-\alpha_0)]\cos\theta\sin i \\ &- [\cos\delta\cos\delta_0\cos(\alpha-\alpha_0) + \sin\delta\sin\delta_0]\cos i\}^{-1} \end{aligned} \quad (2)$$

where (α_0, δ_0) is the central coordinate of the LMC, i is the disk inclination, R_{LMC} is the heliocentric distance to the LMC centre, and θ the position angle (PA) of the minor axis. In the reference frame adopted here, the inclination i has negative values when the North side of the LMC is closer to us. In the reference frame adopted, the i angle is reversed to what is typically adopted in the literature.

The density of stars is simply given by

$$\rho(\alpha,\delta) = \rho_0 t(\alpha,\delta)^2 exp(-R/R_s) + \rho_{BG} f(\alpha,\delta) \quad (3)$$

where R is the radial distance in the disk plane, R_s is the scale length of the exponential disk, $\rho_0 t(\alpha_0, \delta_0)$ is the central density, and ρ_{BG} is the density of background/foreground stars. The function $f(\alpha, \delta)$ is a third degree polynomial which takes into account the spatial variation of MW field stars.

Five parameters are used to model the disk geometry: the LMC central coordinates (α_0, δ_0), its distance to the Sun (R_{LMC}), the inclination i, and the PA θ. Additionally, 3 parameters describe the density of stars along this disk: the central density ρ_0, the scale radius R_s, and the density scale of background stars ρ_{BG}.

To simplify the problem and to better accommodate the fact that the observations are all on the northern side of the MCs, we make a few assumptions. The LMC centre is kept fixed at the Nikolaev et al. (2004) value of $(\alpha_0, \delta_0) = (79.40°, -69.03°)$. The heliocentric distance to the LMC centre $R_{LMC} = 49.9$ kpc is adopted from the most recent review about the subject (de Grijs, Wicker & Bono 2014).

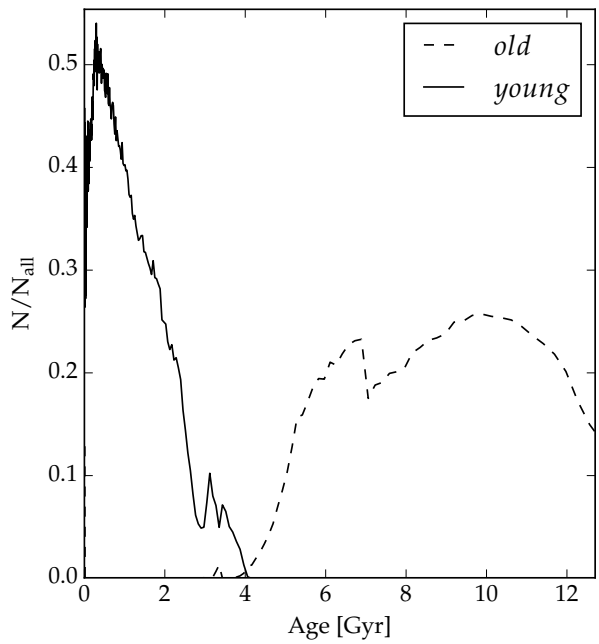

Figure 5. Ratio of the number of *young* (*old*) to *all* stars as a function of age. The ratio was computed using a constant SFR and a Piatti & Geisler (2013) AMR.

With the machinery to produce LMC disk models we proceed to a formal fit to the observed distribution of stars in the SPT-E region. This fit was performed on three samples of stars. The selections were made based on PARSEC (Bressan et al. 2012) stellar evolution models. The first is made only of stars older than 4 Gyr, selected using a colour-magnitude cut shown in Figure 4. The second sample selects only stars younger than 4 Gyr. The third sample is made of stars that fall within the limits $17 < g < 23$ and $-0.5 < g - r < 1.0$. We name these samples *old*, *young*, and *all* for simplicity. In Figure 5 we show the ratio of *old* (*young*) and *all* stars for a simulated LMC stellar population that assumes a constant star formation rate (SFR) and a Piatti & Geisler (2013) age-metallicity relation (AMR). Photometric errors were simulated according to Equation 1 and Table 2. We observe that the colour-magnitude cuts chosen are able to create two samples with virtually no age overlap.

Using a TRILEGAL (Girardi et al. 2005) simulation, we modeled the expected MW stellar population in the SPT-E region. Assuming the same colour cuts as the ones used to select the three stellar populations quoted above, we fit the density of stars as a function of RA and Dec using a third order polynomial, $f(\alpha, \delta)$. The best-fit polynomial for each of the stellar populations cuts is later used to account for foreground contamination while fitting the LMC disk. This polynomial is scaled by $\rho_{\rm BG}$ since the colour-magnitude cuts are not perfectly consistent with the theoretical prediction of TRILEGAL.

To count stars in the sky plane we adopt the HEALPIX

pixelization scheme with $N_{side} = 512$ which yields a constant pixel area across the sky of ~ 0.013 deg^2. The maps built in this scheme for each stellar sample described above are shown in the left panel of Figures 6, 7, and 8.

The best-fit disk model was obtained through a Markov Chain Monte Carlo (MCMC) technique. We used the code EMCEE (Foreman-Mackey et al. 2013) in its version 2.0.0. The test statistics chosen is a binned Poisson log-likelihood model (Dolphin 2002). We refer the reader to these authors for details on the MCMC and statistics used. This is the most appropriate test statistics for data-model comparison since we are dealing with counts that are subject to shot noise, especially in the outermost regions of the LMC. Our MCMC run uses a total of 30 walkers that make 1000 steps each for the *burn-in* phase. After the *burn-in*, we let the walkers advance 5000 more steps each, sufficient to well sample the parameter space and converge to the maxima.

This fitting procedure was repeated for each stellar population (*all, old* and *young*), yielding the parameters shown on Table 3. In this table we chose to present the PA of the line of nodes $\theta_0 = \theta + 90°$. This is the quantity most often presented in the literature.

The boxes chosen to select a given stellar population in the colour-magnitude diagram (CMD) assume that the stars are all at the same distance to us. This is not strictly the case for the LMC stars, which are spread across a disk plane inclined relative to the sky plane. To test how this distance spread affects our disk fit we correct the magnitude of each star using the best-fit disk models so as to bring the stars to a common distance. This common distance is chosen as the mean distance to the disk in the SPT-E. Using these distance corrected magnitudes we perform the CMD box selections again. For all the CMD based selections an increase of $< 1\%$ in the number of stars inside the CMD box is observed. Using this distance corrected sample we rerun the fitting procedure and find that the largest change in the parameters is a 5% increase in the inclination. The remaining disk parameters are more stable. We adopt the difference on the parameters found in this experiment as the systematic uncertainty in our parameter estimation. We show this variations as the uncertainties in parenthesis in Table 3.

The left panel of Figure 6 a HEALPIX map in Gnomonic projection shows the logarithm of the number of stars for the *all* stellar population. Overploted we show the best-fit disk model as isodensity lines. On the right side of the figure we show the sampled probability distribution function for each parameter after marginalization. In light blue we mark the point of maximum probability density, which indicates the maximum likelihood solution. Notice that the samples are distributed in a fairly symmetric way around the maxima, yielding symmetric error bars. On Figures 7 and 8 are similar to the figure described above, but showing different age-selected populations.

We notice that the *old* population spreads out to declinations of $\sim -55°$, while the *young* population is much more abruptly truncated at $\sim -60°$. This points to different scale radii for these populations. In Table 3 we give a summary of the parameters that best-fit each case. Here we see that the distributions have significantly different values of R_s while retaining similar values for the purely geometrical parameters θ_0 and i.

The difference in the scale length is much more obvious in Figure 9 where we show, for each stellar population, the average number of stars per HEALPIX pixel in bins of distance along the LMC disk. We also show the best-fit disk model for each of the stellar populations, this model includes the MW foreground stars (i.e. the term $\rho_{\rm BG} f(\alpha, \delta)$ in Equation 2). We notice that the *old* (triangles and dot-dashed line) profile is much more extended than the *young* one (crosses and dotted line). It is also remarkable that the LMC *old* density profile is well fit without the need for other components such as a spheroidal halo. However, the *young* profile is not very well described by the disk model. This could also account for the value found for its inclination, which is not in good agreement with the literature (van der Marel & Cioni 2001; Nikolaev et al. 2004; Rubele et al. 2012). In the same figure, the solid line shows the contribution of MW stars, we notice that the slope in the number of stars at the outskirts of the LMC can be accounted by for the spatial variation in the number of MW field stars. Due to the large number of stars in each radial bin, the Poisson uncertainty is very low. These uncertainties are only visible, as error bars, on the inset plot, where the outer parts of the *old* population profile is shown.

We notice from Table 3 that the statistical uncertainties in the disk parameters are quite small. This is caused by the relatively poor description that our disk model gives of the LMC stellar population, especially the *young* population. In Figure 9 this becomes apparent where we observe that the models deviate significantly from the observations, even when the uncertainties are considered. This can point to the case where there are other systematic effects that were not taken into account. One cause of such effects might be the spatial variation of the star-galaxy classifier. However, the classifier adopted here is very stable especially at bright magnitudes ($g < 22.5$), thus being improbable to be a significant source of error. Also, spatial changes in the completeness of the survey are unlikely to cause a large change in the number of stars per HEALPIX pixel (see Section 3.3). Evidence indicates that the deviations from the fitted disk model are real features of the LMC structure. These features are more apparent for the *young* stellar population, which is most likely to hold signs of disk perturbations such as spiral arms.

We use the *old* population profile to probe the total extent of the LMC. We define the truncation radius as the radius where the observed density profile reaches becomes indistinguishable from the MW foreground population. In the inset plot of Figure 9 we observe that for $\log(R/kpc) > 1.13$ the profile can be explained solely by the MW contribution. The uncertainty on this truncation radius ($R_{\rm t}$) is taken as the size of the radial bin, which is 0.8 kpc. This yields a $R_{\rm t} = 13.5 \pm 0.8$ kpc.

If we assume that the LMC luminous component is tidally truncated by the MW potential we can use the simple theoretical tidal radius formula (Binney & Tremaine 2008), given by:

$$R_{\rm t} = d_{\rm LMC} \left(\frac{M_{\rm LMC}}{2M_{\rm MW}(d < d_{\rm LMC})} \right)^{\frac{1}{3}} \quad (4)$$

we find the following relation for the LMC mass ($M_{\rm LMC}$) and the MW mass ($M_{\rm MW}$) encircled within a radius equal

Population	Age Gyr	θ_0 deg	i deg	R_s kpc	ρ_0 stars pixel^{-1} kpc^{-2}	ρ_{BG}
All	–	$129.51 \pm 0.17(\pm 1.08)$	$-38.14 \pm 0.08(\pm 1.59)$	$1.09 \pm 0.01(\pm 0.02)$	$26.41 \pm 0.14(\pm 0.59)$	$0.80 \pm 0.03(\pm 0.67)$
Young	0 - 4	$125.93 \pm 0.20(\pm 0.09)$	$-44.19 \pm 0.14(\pm 1.80)$	$0.72 \pm 0.01(\pm 0.00)$	$22.86 \pm 0.28(\pm 1.33)$	$9.06 \pm 0.18(\pm 0.00)$
Old	4 - 13	$127.40 \pm 1.02(\pm 0.59)$	$-32.94 \pm 0.39(\pm 1.25)$	$1.41 \pm 0.01(\pm 0.00)$	$0.89 \pm 0.02(\pm 0.05)$	$2.08 \pm 0.04(\pm 0.01)$

Table 3. A summary of the best-fit disk models parameters for each stellar population. The uncertainties are the 3σ confidence level that arises from the MCMC analysis. The uncertainties in parenthesis are obtained from the difference between the fit with and without correcting the magnitudes by the heliocentric distance to each point of the LMC disk. NOTE: our definition of inclination (i) has the opposite sign than what is typically found in literature.

to the Galactocentric distance of the LMC ($d_{\rm LMC}$):

$$M_{\rm MW}(d < d_{\rm LMC}) = 24.5^{+8.8}_{-6.4} \times M_{\rm LMC} \quad (5)$$

where the Sun is assumed to be at a distance of $d_\odot = 8.0$ kpc from the MW centre. This yields a $d_{\rm LMC}$ of 49.4 ± 2.1 kpc. The uncertainty in this value was considered for the result in Equation 5. The distance to the Sun is taken as a compromise between two recent determinations from Eisenhauer et al. (2005) and Gillessen et al. (2009). The adoption of $d_\odot = 8.5$ kpc would increase $d_{\rm LMC}$ by $\sim 0.03\%$, leading to an insignificant increase in $R_{\rm t}$. Thus, we choose to disregard the uncertainty in $d_\odot$.

To further support our claim that there are very few LMC stars beyond 13 kpc we show in Figure 10 the Hess diagrams at different bins of angular separation from the LMC centre. The upper and lower bound of each bin is indicated in each panel. We apply a simple decontamination algorithm in order to remove the contribution of MW stars. The decontamination was done by selecting a region with angular distance greater than $\theta = 20°$. A Hess diagram of this region was constructed. These Hess diagrams were area weighted and subtracted from the Hess diagram of each angular separation bin shown in Figure 10. This process assumes that the contribution of LMC stars at angular distances larger than 20° is negligible. We again assume that the MW stellar population varies very little throughout the SPT-E.

In Figure 10 we note, from visual inspection, that the LMC population in the bottom central panel is indistinguishable from the noise in the Hess diagram. This panel corresponds to angular separations between 15° and 16°. This range corresponds to distances from 10.5 and 11.2 kpc along the disk plane, which are intermediate between the truncations radius of the *old* and *young* population. This does not mean the complete absence of LMC stars. However, it shows that at this range of distances the LMC populations is too low in number to be distinguishable by eye from the MW foreground stars.

With the aid of the GALPY[1] (Bovy 2010) suite for galactic dynamics we compute a three component MW potential with a NFW halo (Navarro, Frenk & White 1996), a Miyamoto-Nagai disk (Miyamoto & Nagai 1975), and a Hernquist bulge (Hernquist 1990) following the same recipe as in Bovy et al. (2012). This potential was normalized such as to yield a Solar circular velocity of 220 km/s at the Galactocentric distance of 8 kpc. We obtain that the enclosed MW mass inside a sphere centred in the MW with radius d_{LMC} is $5.6 \times 10^{11} M_\odot$. Using the result from Equation 5 and propagating the uncertainties in R_t we obtain an LMC mass of $M_{LMC} = 2.3^{+0.8}_{-0.6} \times 10^{10} M_\odot$.

According to the set of simulations by Kallivayalil et al. (2013), the combination of MW and LMC masses found in this work would favor a scenario where the Magellanic System is in its first pericentric passage. However, it is not clear if there is enough time for the LMC to develop a truncation radius without finishing a complete orbit around the MW and if this truncation would affect its luminous component. We would like to stress that the calculations presented in our work are subject to many uncertainties, especially with respect to our knowledge of the MW mass profile at large distances.

5 THE LMC RED CLUMP AS A DISTANCE ESTIMATOR

The peak magnitude of the RC is used widely in astronomy as a standard candle to determine distances of old and intermediate age star clusters. RC stars are He-burning stars of mass $M \lesssim 2M_\odot$; they develop an electron degenerate core after the main sequence, and as a consequence have to increase their core up to a critical mass of $\sim 0.46 M_\odot$ before Helium can be ignited. The almost-constancy of their Helium-core masses determines that they all share similar (but not constant) luminosities in their central helium burning phase.

Using the RC peak magnitude as a standard candle we define the distance modulus μ_0 with the following equation:

$$\mu_0 = m_\lambda^{RC} - M_\lambda^{RC} - A_\lambda - \Delta M_\lambda^{RC} \quad (6)$$

where A_λ is the extinction, M_λ^{RC} is the absolute magnitude of the RC peak, and ΔM_λ^{RC} is a correction in the absolute magnitude due to population mixing effects. Here λ represents the observational filters ($\lambda = g, r, i, z$).

If one is to determine μ_0, the terms A_λ and ΔM_λ^{RC} must be inferred. Here we choose to correct the magnitudes for extinction using the Schlegel, Finkbeiner & Davis (1998) dust maps. For the time being we will assume that ΔM_λ^{RC} is zero. This assumption will be addressed in more detail later.

To probe μ_0 as a function of position in the LMC, we subdivided the sky in HEALPIX pixels using the pixelization scheme with $N_{side} = 128$. This gives a pixel area of ~ 0.21 deg^2. We choose a larger pixel than the previous section since the RC is much less populated than the Main Sequence. To measure the peak apparent magnitude of the RC in a given

[1] http://github.com/jobovy/galpy

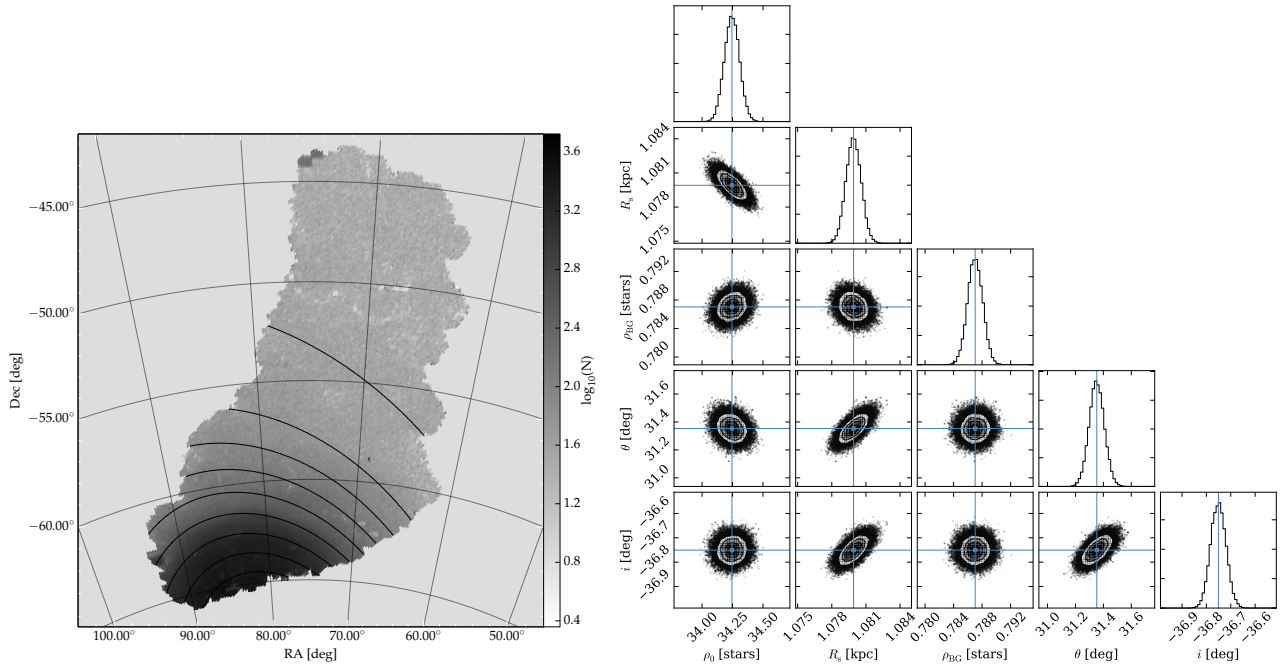

Figure 6. *Left panel:* map showing the number of stars from the *all* sample in grayscale. The stars used to build this map are those that fall inside a simple color cut of $-0.5 < g - r < 1.0$ and $g < 23$. The solid isodensity contours show the best exponential disk model. The contours start at $\log_{10}(N) = 3.3$ and progress in steps of 0.3 dex. *Right panels:* the marginalization for the different disk model pairs of parameters. The solid blue crosshair shows the position of the best solution. The contours show the 1, 2, and 3σ confidence levels. The histograms in the diagonal panels show the marginalization over each single parameter. Again the blue line shows the point of maximum likelihood.

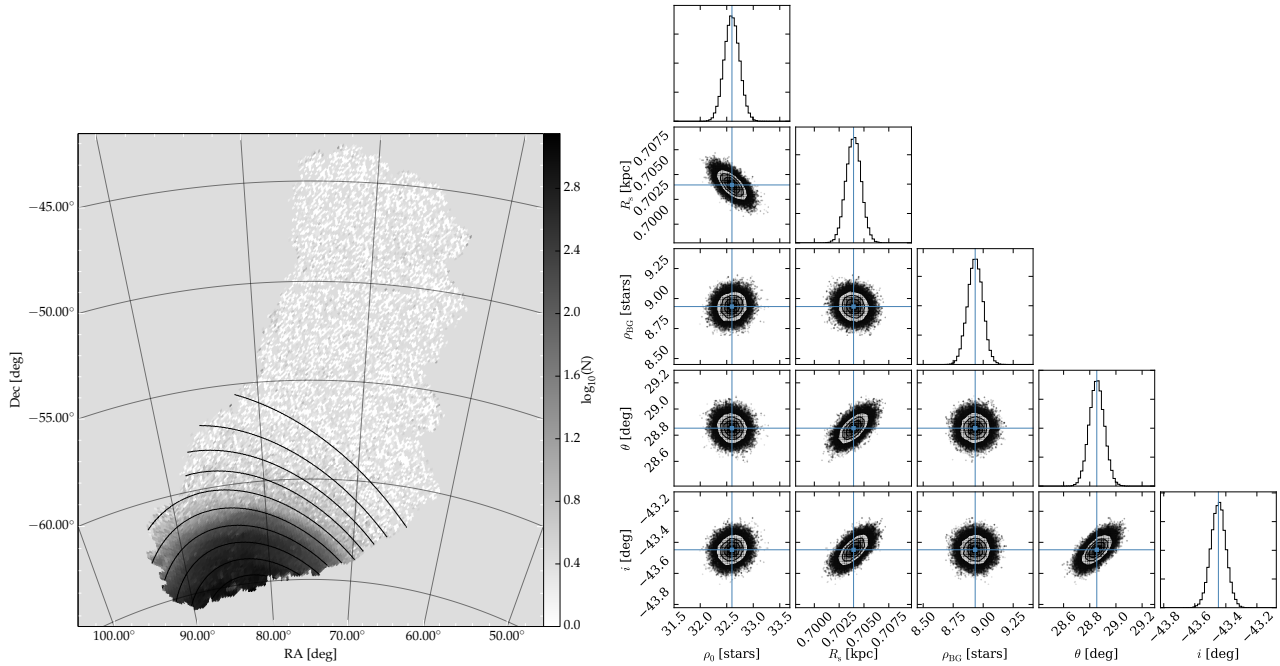

Figure 7. Similar to Figure 6 but for the *young* stellar population. The isodensity contours start at $\log_{10}(N) = 2.9$ and progress in steps of 0.4 dex.

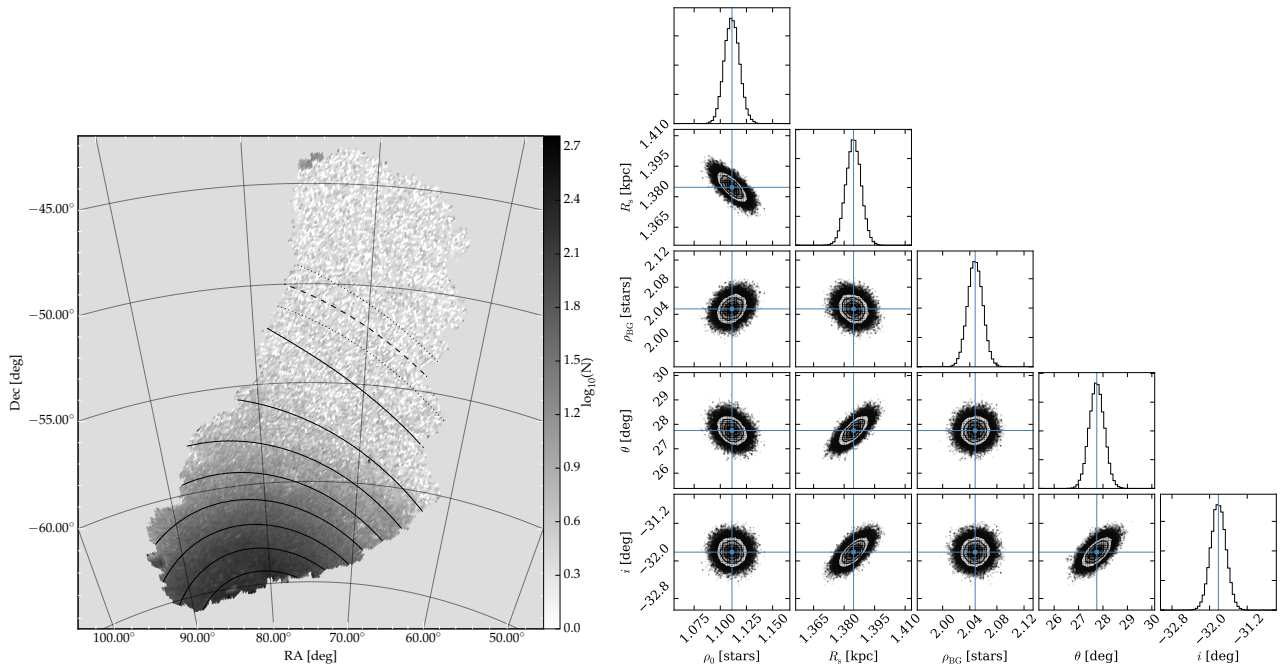

Figure 8. Similar to Figure 6 but for the *old* stellar population. The isodensity contours start at $\log_{10}(N) = 2.5$ and progress in steps of 0.35 dex. In the left panel we also show the truncation radius ($R_{\rm t}$) position as the dashed contour, and the dotted contours show the uncertainty in $R_{\rm t}$.

passband (m_λ^{RC}) we compute the number count of stars as a function of magnitude ($N(m_\lambda)$) for stars that have colours and magnitudes limited by the dashed boxes in Figure 4. The CMD region occupied by RC stars was selected visually.

To build $N(m_\lambda)$ the bin size is chosen according to the method described in Knuth (2006), which is based on optimization of a Bayesian fitness function across fixed-width bins. This avoids issues that may arise from oversampling or undersampling the number of bins. The values of $N(m_\lambda)$ are fitted by means of a non-linear least square algorithm using a second order polynomial plus a Gaussian. This function is given by the following equation:

$$N(m_\lambda) = a + bm_\lambda + cm_\lambda^2 + d\exp\left[\frac{-(m_\lambda^{RC} - m_\lambda)^2}{2\sigma_\lambda^2}\right] \qquad (7)$$

where a, b, c are the coefficients of the polynomial, d is the normalization of the Gaussian and σ_λ is the standard deviation of the magnitudes around the RC peak.

The uncertainty on m_λ^{RC} is taken from the covariance matrix of the least square fit.

It is convenient to define the heliocentric distance to points in the LMC disk as a function of the so called line of maximum distance gradient. This line connects points on the disk plane with the most rapidly varying distance from us, hence its name. The distance along this line is the deprojected distance between a point in the disk to the line of nodes. The distances along this line are given by the y component of Equation A3 of Weinberg & Nikolaev (2001). The line of maximum distance gradient has a PA given by θ (Equation 2) and it is oriented approximately in the NE-SW direction. Showing the heliocentric distance to points in the LMC disk as a function of the position in the line of maximum distance gradient is the equivalent of showing an edge-on view of the LMC.

To infer the absolute magnitude of the RC (M_λ^{RC}) we could adopt the prediction from synthetic stellar populations based on stellar evolution models. However, simulations using PARSEC (Bressan et al. 2012) models agree well with the disk models found in this work. A small magnitude offset can be seen on Figure 11, where the solid black line shows the best-fit disk model and the gray points are the inferred distance modulus based on theoretical values of M_λ^{RC}.

Despite the small offset in the theoretical value of M_λ^{RC} we chose to determine M_λ^{RC} by matching the expected distance modulus from our best-fit disk model to the observed values of the RC peak magnitude. This matching was done using stars that are between 3 and 4 kpc along the LMC line of maximum distance gradient. We compute the median value of m_λ in this distance range and subtract from that the heliocentric distance expected from the disk model at 3.5 kpc from the LMC centre. This offset is determined for all passbands. The value obtained is then used to compute the RC-based distances consistently with our disk model. These distances are shown as the black points in Figure 11 and the error bars are propagated from the RC peak fit.

In Figure 12 we show the distributions of m_λ^{RC} on the sky, for $\lambda = g$, r, i, z. The lines show the direction of maximum gradient and the line of nodes obtained from our best disk model fit using the *all* stellar population. We notice that the entire sampled region in this work is on the same side (near side) of the LMC disk major axis. There is a global trend in the sense that for all passbands the nearest points to us are located in the North-East edge of the LMC. Another remarkable feature present in all maps is that the North edge of the LMC is systematically more distant than

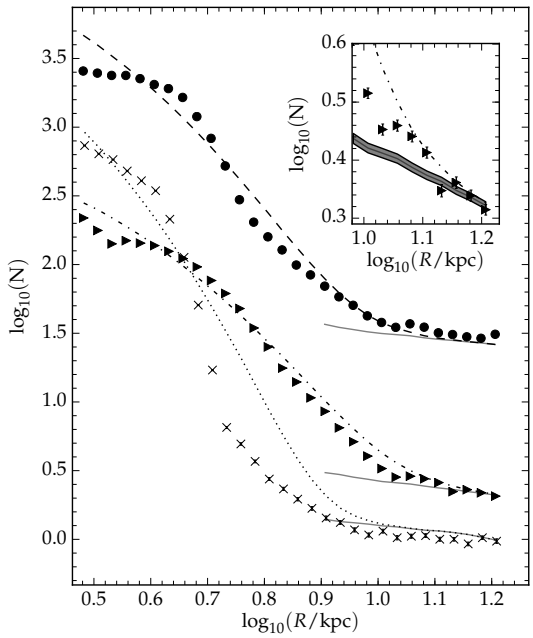

Figure 9. The black circles show the averaged number of stars from the *all* sample per HEALPIX pixel in different bins of distances along the LMC disk. The triangles (crosses) show the same but for the *old* (*young*) sample. The dashed, dot-dashed, and dotted lines show the best-fit disk model for the *all, old,* and *young* populations, including the term $\rho_{BG} f(\alpha, \delta)$ that accounts for the contamination of MW stars. In the inset plot we show the outer tail of the *old* profile. The solid line shows the MW contribution and the shaded region shows its uncertainty, propagated from the uncertainty in $\rho_{\rm BG}$. The errobar represents the Poission uncertainty on the number of counts per bin.

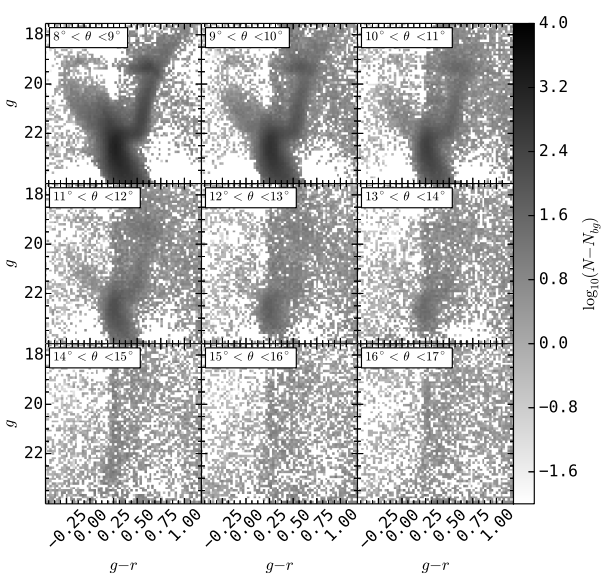

Figure 10. Hess diagrams in $g - r$ vs. g for different angular distance ranges (indicated in the top left of each panel). The contribution from MW stars has been removed as described in the text.

what is expected for the disk model. This effect is noticeable in all passbands.

The discrepancies observed in the maps described above may be due to population mixing in RC stars. The RC luminosity depends slightly on the age and metallicity of the stars (Girardi 1999; Girardi & Salaris 2001). This fact makes the RC of a stellar population older than ~ 3 Gyr dimmer as a function of age. The exact amount of dimming depends on the metallicity and on the passband used. A detailed discussion about how the RC magnitude of simple stellar populations (SSP) varies with age and metallicity may be found in Girardi & Salaris (2001).

In the case of the LMC we would like to know how the RC magnitude changes as a function of the SFH, therefore mapping ΔM_λ^{RC} at different positions in the LMC. However, it is known that the LMC SFH is very complex and varies spatially (Meschin et al. 2014), therefore rendering this a very difficult task.

To assess the amplitude of the populations mixing effect over the RC magnitudes, we conducted a series of synthetic stellar population experiments. These simulations assume that the LMC follows an age-metallicity relation given by Piatti & Geisler (2013) with a spread of 0.15 dex in $[Fe/H]$. We also assume that stars in the LMC follow a Kroupa Initial Mass Function (IMF) (Kroupa 2001). To generate synthetic magnitudes for a set of simulated stars we adopt the PARSEC (Bressan et al. 2012) isochrones in the DES photometric system. Our grid of models has a step of 0.01 in $\log_{10}(age/yr)$ and 0.0002 in Z in the range $[0.0002, 0.001]$ and 0.001 for Z in the range $[0.001, 0.020]$. Photometric uncertainties were included according to Equation 1 and Table 2. The simulations were made in the framework of the open-source code GENCMD[2]

We adopt three SFHs that are modelled according to what has been found by Meschin et al. (2014) for the outer regions of the LMC (red squares in Figure 12). The simulated SFHs contain two events of star formation that were modelled as Gaussian peaks in SFR. The young peak is centered on an age of 2.5 Gyr with a width of 1 Gyr while the second is centered on 9 Gyr with a width of 1.5 Gyr. The first adopted SFH gives equal amplitude to each star forming event, the second gives twice the amplitude to the older event, and the third gives twice the amplitude to the younger event. The largest difference for the RC peak magnitude was observed between the models with asymmetric peaks in the SFH. We use this difference to estimate the maximum value for ΔM_λ^{RC} which was found to be 0.06, 0.06, 0.07, and 0.11 for g, r, i, z respectively. The dashed lines in Figure 11 show the maximum expected deviations due to populations mixing effects.

We notice that the RC distance variations are very similar to the one expected from the best-fit disk model. However there are very discrepant points that the disk model cannot account for, even when population mixing effects are considered. We also notice that the distance moduli determined using different passbands are consistent.

From the RC distributions we may also extract information about the thickness of the LMC disk. This information is embedded in σ_λ shown in Equation 7. However, this quan-

[2] `https://github.com/balbinot/genCMD`

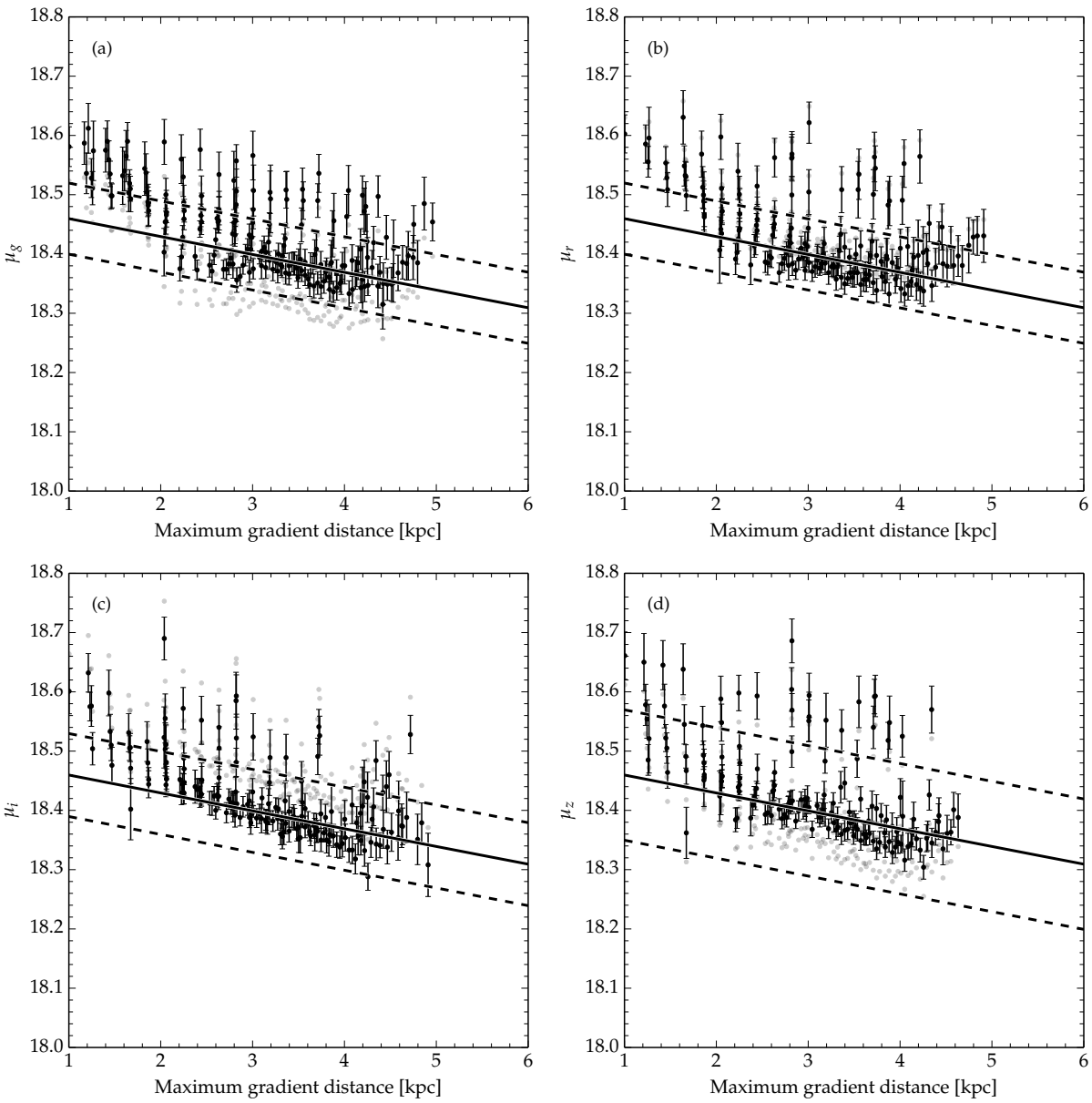

Figure 11. The distance modulus as a function of the distance along the maximum gradient line ($\sim$ NE-SW). The black circles are the measured distance modulus in each HEALPIX pixel, as describe in the text. The error bars shows the 1 σ_m for each measured point. The solid line shows the behaviour expected from the best-fit disk model for the *all* population. The dashed line shows the maximum magnitude variation expected from populations mixing effects. The gray points are the distance modulus inferred using the theoretical RC absolute magnitude. Panels a,b,c, and d show the distance modulus determination using the filters g, r, i, and z respectively.

tity is also affected by the intrinsic scatter of the RC and by photometric uncertainty. The RC simulations described above incorporate this intrinsic scatter (σ_i) convolved with the photometric one (σ_{phot}). In our simulations we measure this quantity ($\sqrt{\sigma_i^2 + \sigma_{phot}^2}$) and we find that this quantity has a mean value of 0.11, 0.12, 0.13, 0.13 for g, r, i, and z respectively. Finally the last contributions comes from the depth of the disk along the line of sight itself (σ_{depth}). Thus, we may write:

$$\sigma_{depth}^2 = \sigma_\lambda^2 - \sigma_{phot}^2 - \sigma_i^2. \quad (8)$$

In Figure 13 we show σ_{depth} as a function of the distance along the LMC disk. The error bars are taken from the covariance matrix obtained on the least-square fit of the RC distribution as given by Equation 7. We took averages of σ_{depth} in bins of 0.5 kpc, which are shown as the black circles. The error bar is the standard deviation of the values of σ_{depth} in each distance bin. For distances less than $\sim$ 4.5 kpc we observe a constant depth of $\sim$ 0.08 mag (1.8 kpc) measured in r, i, and z while the g band yields a value of 0.12 mag (2.8 kpc). The depth in r, i, and z passbands tends to increase by $\sim$ 0.02 mag ($\sim$ 0.5 kpc) towards the edge of the LMC. The slight difference in the g band depth might be due to the underestimate of the intrinsic RC magnitude spread. This effect may be due to changes in the metallicity

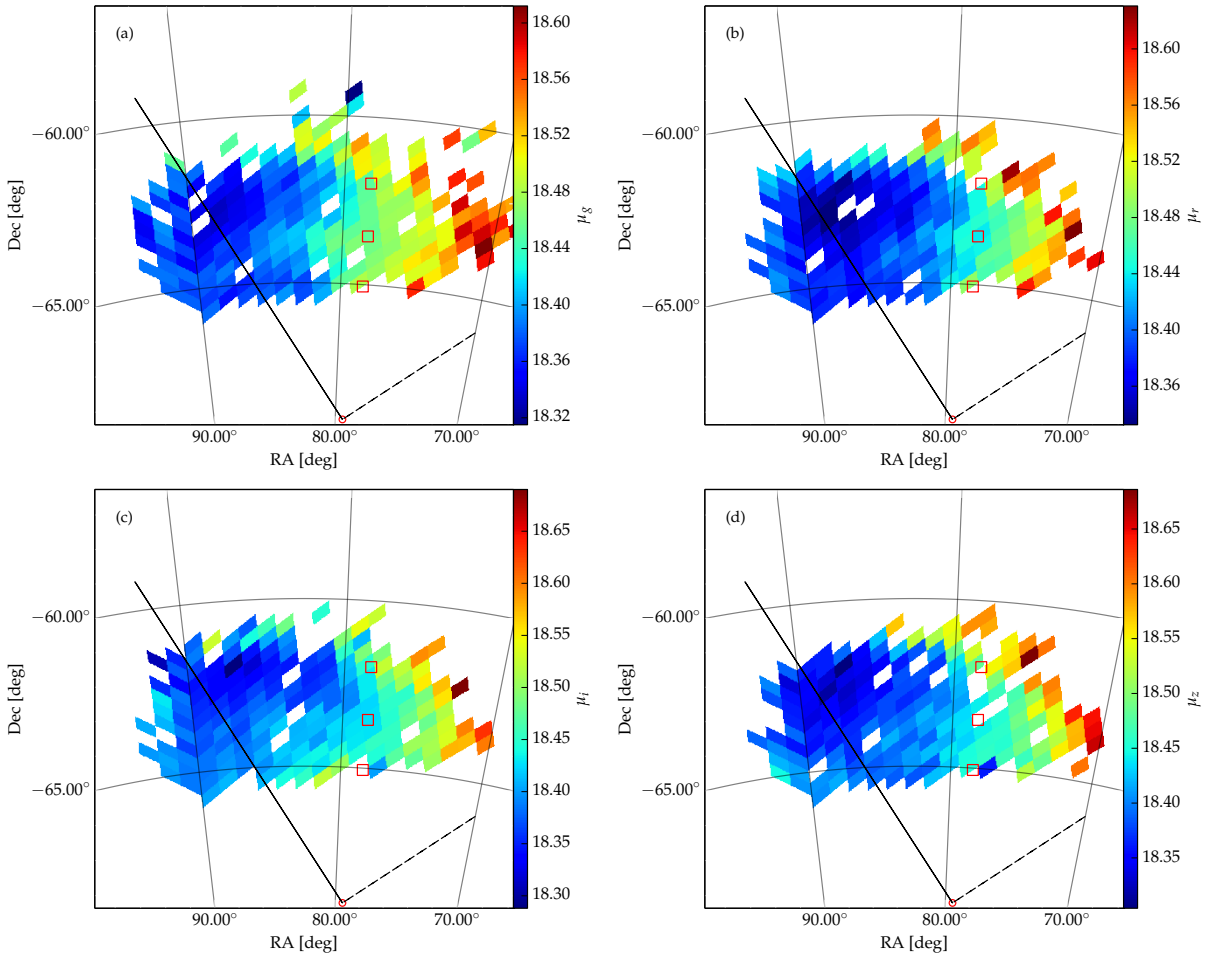

Figure 12. Gnomonic projection of $N_{side} = 128$ maps showing the distance modulus measured in each the g, r, i,and z passband. On every panel the solid line shows the direction of the maximum distance gradient (θ) and the dashed line the direction of the line of nodes (θ_0) expected from the best-fit disk model for the *all* population. The red squares are the fields studied by Meschin et al. (2014). The red circle is the LMC centre adopted in this work. Panels a, b, c, and d show the distance modulus determination using the filters g, r, i, and z respectively.

of the LMC field populations towards its edge (Majewski et al. 2009), leading to the formation of a Horizontal Branch (HB) instead of a RC. The g band is more affected since it is more sensitive to hotter stars.

6 DISCUSSION AND SUMMARY

To the best of our knowledge, this paper is the first to show a clear distinction in the structure of the LMC disk for stellar populations of different ages. Meschin et al. (2014) report signs of an age gradient, but did not derive the structural properties for different age components of the LMC. Previous studies, based on large spectroscopic samples, reported a clear kinematic distinction between different stellar types and attributed that to an age difference in their samples (van der Marel, Kallivayalil & Besla 2009, and references therein). Here we confirm this distinction based only on stellar photometry alone.

The disk models obtained in this work are in agreement with what has been reported in the literature (e.g. Rubele et al. 2012; Saha et al. 2010; Nikolaev et al. 2004; Weinberg & Nikolaev 2001). We observe a significant difference between disk models fitted using stars younger and older than 4 Gyr. The most striking difference is found in the scale length (R_s), which suggests a star formation that follows the outside-in paradigm. The summary of the disk models parameters can be found in Table 3.

The *young* population is poorly described by an exponential disk model. It presents a prominent feature that strongly deviates from an exponential profile truncated at ∼8 kpc. The *young* and *old* LMC disk have a clear distinction in the level of substructures. The younger stars are known to have peculiar spiral arms that have most likely been formed in the last SMC-LMC encounter (Staveley-Smith et al. 2003; Olsen & Massey 2007; Bekki 2009). This could explain why the *young* disk cannot be well described by our disk model.

On the other hand, the *old* disk extends over ∼ 13 scale lengths. Our results for the scale length and truncation radius are similar to what Saha et al. (2010) found. The authors report $R_s \simeq 1.15$ and a truncation radius that is ∼12 times this value, which is very similar to our determination. If we assume that the truncation radius of the *old* disk is

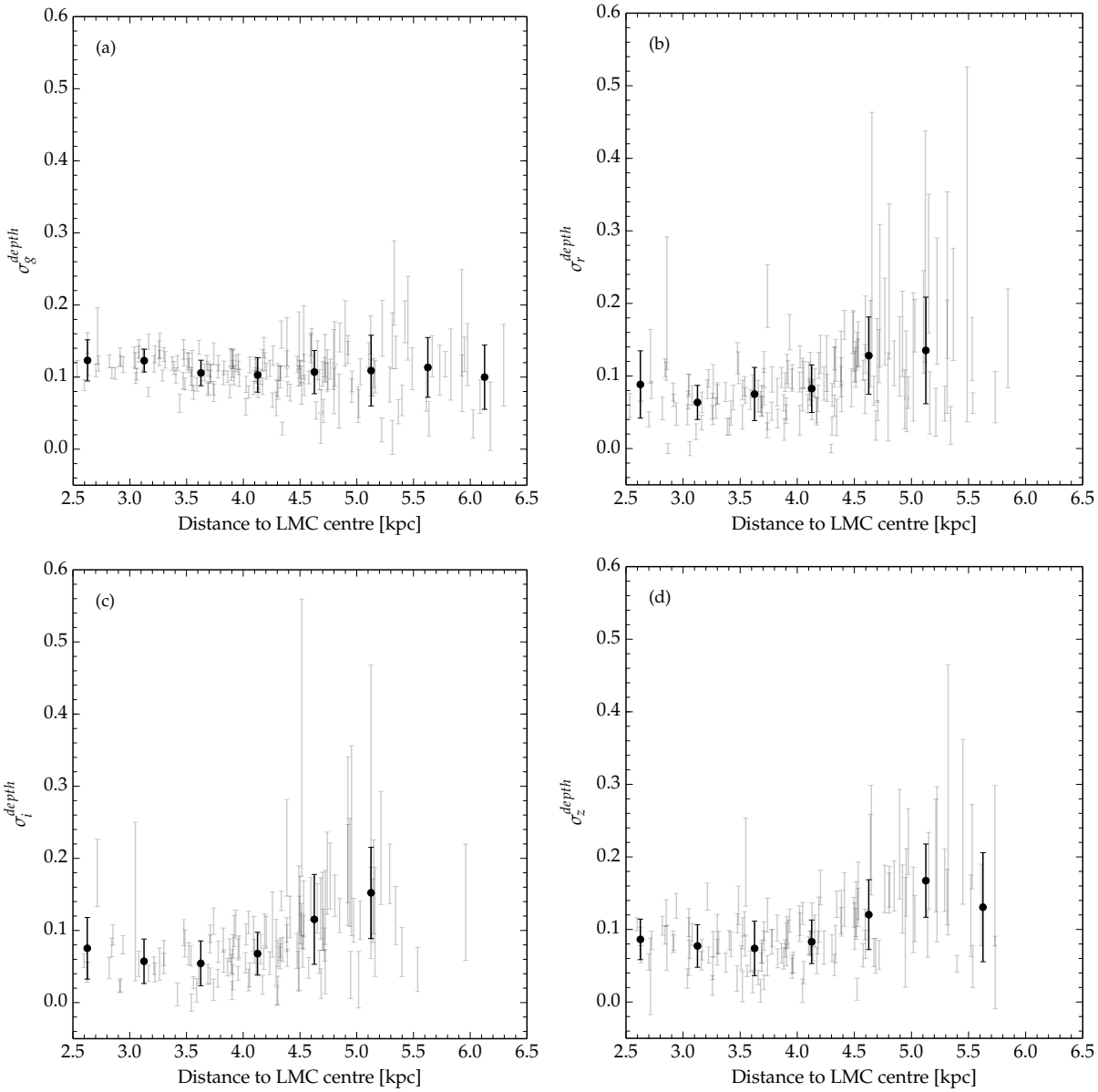

Figure 13. Disk depth as a function of distance to the LMC centre. The gray error bars show the σ_{depth} measured for each HEALPIX pixel shown on Figure 12. The dark circles are the average over 0.5 kpc and the error bar the standard deviation. Panels a,b,c, and d are for determinations using the filters g, r, i, and z respectively.

caused by the tidal field of the MW, we obtain a LMC mass that is $M_{LMC} = 2.3^{+0.8}_{-0.6} \times 10^{10} M_{\odot}$. This mass is strongly dependent on the efficiency with which the MW potential tidally truncates the LMC stellar distribution. Even if the Clouds are in their first pericentric passage, their orbit is predicted to be past the pericenter, which could allow the formation of a tidal limit (Besla, private communication). Also, (Gan et al. 2010) showed that subhalos in their first pericentric passage may undergo substantial mass loss. We also point out that in the case where the MW tidal field efficiently strips the dark matter and luminous components, our estimate of the LMC mass is reliable. However, in the case where dark matter is still present in an extended halo, our estimate of the LMC mass sets only a lower limit. The absolute mass value is also dependent on the MW mass profile, but the relative LMC to MW encircled mass is not. New more precise determinations of the MW mass in its outer regions will help to more accurately constrain the LMC mass.

The dynamical mass determination by van der Marel & Kallivayalil (2014) suggests $M_{LMC}(R < 8.7 \text{ kpc}) = (1.7 \pm 0.7) \times 10^{10} M_{\odot}$ that can be extrapolated to the mass inside our truncation radius of $M_{LMC}(R < R_t) = (3.5 \pm 1.4) \times 10^{10} M_{\odot}$ assuming a flat rotation curve. This value is within the error bars of our mass determination, suggesting that the truncation radius found in this work has a tidal origin.

Through the fit of the RC peak magnitude we observe that a few regions coherently grouped in the North of the LMC are systematically more distant than what is expected by an inclined circular disk model. While Olsen & Salyk (2002) found that regions of the South-East LMC are sys-

tematically closer, we find that the Northern LMC disk behaves in the opposite sense. This is the classic case for a galaxy with warped disk. We demonstrate, through the use of synthetic stellar population models, that the offsets from the disk model are larger than what is expected from population mixing effects.

Using the same synthetic stellar populations quoted above we are able to compute the theoretical magnitude scatter of RC stars. This allows us to disentangle the contribution of the intrinsic scatter from the one caused by the disk thickness. We measure a thickness ranging from 1.8 to 2.8 kpc in the inner parts of the LMC and which increases by 0.5 kpc in its outer parts. If we assume that the disk follows an exponential profile in height we obtain that the scale height ranges from 1.3 to 1.9 kpc, increasing by 0.3 kpc in the outer parts. This slight increase towards the outskirts can be interpreted as the *flaring* of the disk. van der Marel & Cioni (2001) argue that this kind of behaviour is expected if the LMC disk is tidally perturbed by the MW potential. The disk thickening may also be explained solely by LMC dynamical models (Besla et al. 2012), where the old stellar component is expected to form a dynamically hotter component. The fact that we only observe it on the edge of the LMC may be due to the steep truncation of the *young* disk, allowing us to measure a thickness that is dominated by the *old* population only in the LMC outskirts.

The analysis presented in this work points to a scenario where there are two distinct disk components in the LMC. One is composed of old stars (> 4 Gyr) and possesses a smooth, extended profile out to dozens of scale lengths. The second component is composed of younger stars (< 4 Gyr) and appears to be pertubed and much less extended. We find signs of *warp* and *flare* towards the outskirts of the LMC, both of which have been reported previously (Olsen & Salyk 2002; Subramaniam & Subramanian 2009).

An alternative scenario for the disk *warp* and *flare* is the existence of a hot halo composed of *old* stars, while the disk could contain both populations. Because the *old* population is more *spatially* extended, this scenario would explain the outward increase in the thickness of the RC as the *young* disk fades, therefore accounting for the "flare" signal. Besides the *flaring*, the *old* spheroidal component would lead to a systematic variation on the heliocentric distances across the LMC in the sense of bringing them closer to the heliocentric distance of the LMC centre on both sides of the galaxy, also mimicking a *warp* effect.

The fact that the *old* disk is well-fit by a single exponential disk favours the scenario where there is no detectable stellar halo and older stars form a thicker disk. Also the fact that the hot halo has only been possibly detected in the central regions of the LMC (Minniti et al. 2003) raises doubts about the existence of such a stellar component. To investigate the existence of a halo component, a more detailed study must be carried out in the LMC outskirts in order to isolate its extremely sparse stellar population. This kind of study should employ more sophisticated CMD decontamination methods such as the ones used to detect streams and tidal tails (Rockosi et al. 2002).

The upcoming years promise to greatly increase our understanding of the Magellanic system. With the data already observed during the DES SV campaign, we have the ability to study a vast number of LMC star clusters and their 3-dimensional distribution in the galaxy. The field LMC population may also be used to infer a very detailed, and spatially dependent SFH.

Upcoming DES observations will cover a large portion of the Magellanic Stream allowing for the discovery and characterization of its stellar component, if it exists. Additionally, DES will continue to map the outskirts of the LMC and SMC. This novel dataset will certainly reveal some of the many puzzles of the Magellanic system.

ACKNOWLEDGMENTS

This paper has gone through internal review by the DES collaboration.

We are grateful for the extraordinary contributions of our CTIO colleagues and the DECam, Commissioning and Science Verification teams in achieving the excellent instrument and telescope conditions that have made this work possible. The success of this project also relies critically on the expertise and dedication of the DES Data Management group.

Funding for the DES Projects has been provided by the U.S. Department of Energy, the U.S. National Science Foundation, the Ministry of Science and Education of Spain, the Science and Technology Facilities Council of the United Kingdom, the Higher Education Funding Council for England, the National Center for Supercomputing Applications at the University of Illinois at Urbana-Champaign, the Kavli Institute of Cosmological Physics at the University of Chicago, Financiadora de Estudos e Projetos, Fundação Carlos Chagas Filho de Amparo à Pesquisa do Estado do Rio de Janeiro, Conselho Nacional de Desenvolvimento Científico e Tecnológico and the Ministério da Ciência e Tecnologia, the Deutsche Forschungsgemeinschaft and the Collaborating Institutions in the Dark Energy Survey.

The Collaborating Institutions are Argonne National Laboratory, the University of California at Santa Cruz, the University of Cambridge, Centro de Investigaciones Energeticas, Medioambientales y Tecnologicas-Madrid, the University of Chicago, University College London, the DES-Brazil Consortium, the Eidgenössische Technische Hochschule (ETH) Zürich, Fermi National Accelerator Laboratory, the University of Edinburgh, the University of Illinois at Urbana-Champaign, the Institut de Ciencies de l'Espai (IEEC/CSIC), the Institut de Fisica d'Altes Energies, Lawrence Berkeley National Laboratory, the Ludwig-Maximilians Universität and the associated Excellence Cluster Universe, the University of Michigan, the National Optical Astronomy Observatory, the University of Nottingham, The Ohio State University, the University of Pennsylvania, the University of Portsmouth, SLAC National Accelerator Laboratory, Stanford University, the University of Sussex, and Texas A&M University.

The DES participants from Spanish institutions are partially supported by MINECO under grants AYA2009-13936, AYA2012-39559, AYA2012-39620, and FPA2012-39684, which include FEDER funds from the European Union.

DG was supported by SFB-Transregio 33 'The Dark Universe' by the Deutsche Forschungsgemeinschaft (DFG)

and the DFG cluster of excellence 'Origin and Structure of the Universe'.

JZ acknowledges support from the European Research Council in the form of a Starting Grant with number 240672.

REFERENCES

Alves D. R., 2004, ApJ, 601, L151
Balbinot E., Santiago B., Girardi L., da Costa L. N., Maia M. A. G., Pellegrini P. S. S., Makler M., 2012, in Astronomical Society of the Pacific Conference Series, Vol. 461, Astronomical Data Analysis Software and Systems XXI, Ballester P., Egret D., Lorente N. P. F., eds., p. 287
Balbinot E., Santiago B. X., Bica E., Bonatto C., 2009, MNRAS, 396, 1596
Bekki K., 2009, in IAU Symposium, Vol. 256, IAU Symposium, Van Loon J. T., Oliveira J. M., eds., pp. 105–116
Bertin E., 2006, in Astronomical Society of the Pacific Conference Series, Vol. 351, Astronomical Data Analysis Software and Systems XV, Gabriel C., Arviset C., Ponz D., Enrique S., eds., p. 112
Bertin E., 2011, in Astronomical Society of the Pacific Conference Series, Vol. 442, Astronomical Data Analysis Software and Systems XX, Evans I. N., Accomazzi A., Mink D. J., Rots A. H., eds., p. 435
Bertin E., Arnouts S., 1996, A&AS, 117, 393
Bertin E., Mellier Y., Radovich M., Missonnier G., Didelon P., Morin B., 2002, in Astronomical Society of the Pacific Conference Series, Vol. 281, Astronomical Data Analysis Software and Systems XI, Bohlender D. A., Durand D., Handley T. H., eds., p. 228
Besla G., Kallivayalil N., Hernquist L., van der Marel R. P., Cox T. J., Kereš D., 2012, MNRAS, 421, 2109
Binney J., Tremaine S., 2008, Galactic Dynamics: Second Edition. Princeton University Press
Bouy H., Bertin E., Moraux E., Cuillandre J.-C., Bouvier J., Barrado D., Solano E., Bayo A., 2013, A&A, 554, A101
Bovy J., 2010, ApJ, 725, 1676
Bovy J., Rix H.-W., Liu C., Hogg D. W., Beers T. C., Lee Y. S., 2012, ApJ, 753, 148
Bressan A., Marigo P., Girardi L., Salasnich B., Dal Cero C., Rubele S., Nanni A., 2012, MNRAS, 427, 127
Busha M., 2014, in prep.
Cardelli J. A., Clayton G. C., Mathis J. S., 1989, ApJ, 345, 245
Carlstrom J. E. et al., 2011, PASP, 123, 568
Cioni M.-R. L. et al., 2011, A&A, 527, A116
de Grijs R., Wicker J. E., Bono G., 2014, AJ, 147, 122
de Vaucouleurs G., Freeman K. C., 1972, Vistas in Astronomy, 14, 163
Desai S. et al., 2012, ApJ, 757, 83
Dolphin A. E., 2002, MNRAS, 332, 91
Eisenhauer F. et al., 2005, ApJ, 628, 246
Flaugher B., 2005, International Journal of Modern Physics A, 20, 3121
Flaugher B. L. et al., 2010, in Society of Photo-Optical Instrumentation Engineers (SPIE) Conference Series, Vol. 7735, Society of Photo-Optical Instrumentation Engineers (SPIE) Conference Series
Foreman-Mackey D., Hogg D. W., Lang D., Goodman J., 2013, PASP, 125, 306
Fukugita M., Ichikawa T., Gunn J. E., Doi M., Shimasaku K., Schneider D. P., 1996, AJ, 111, 1748
Gan J., Kang X., van den Bosch F. C., Hou J., 2010, MNRAS, 408, 2201
Gillessen S., Eisenhauer F., Fritz T. K., Bartko H., Dodds-Eden K., Pfuhl O., Ott T., Genzel R., 2009, ApJ, 707, L114
Girardi L., 1999, MNRAS, 308, 818
Girardi L., Groenewegen M. A. T., Hatziminaoglou E., da Costa L., 2005, A&A, 436, 895
Girardi L., Salaris M., 2001, MNRAS, 323, 109
Glazebrook K., Peacock J. A., Collins C. A., Miller L., 1994, MNRAS, 266, 65
Górski K. M., Hivon E., Banday A. J., Wandelt B. D., Hansen F. K., Reinecke M., Bartelmann M., 2005, ApJ, 622, 759
Grcevich J., Putman M. E., 2009, ApJ, 696, 385
Hernquist L., 1990, ApJ, 356, 359
Hindman J. V., Kerr F. J., McGee R. X., 1963, Australian Journal of Physics, 16, 570
Holtzman J. A. et al., 1999, AJ, 118, 2262
Javiel S. C., Santiago B. X., Kerber L. O., 2005, A&A, 431, 73
Jensen J., Mould J., Reid N., 1988, ApJS, 67, 77
Kallivayalil N., van der Marel R. P., Besla G., Anderson J., Alcock C., 2013, ApJ, 764, 161
Kelly P. L. et al., 2014, MNRAS, 439, 28
Kerber L. O., Santiago B. X., 2009, in IAU Symposium, Vol. 256, IAU Symposium, Van Loon J. T., Oliveira J. M., eds., pp. 391–396
Klypin A., Kravtsov A. V., Valenzuela O., Prada F., 1999, ApJ, 522, 82
Knuth K. H., 2006, Optimal Data-Based Binning for Histograms
Kron R. G., 1980, ApJS, 43, 305
Kroupa P., 2001, MNRAS, 322, 231
Majewski S. R., Nidever D. L., Muñoz R. R., Patterson R. J., Kunkel W. E., Carlin J. L., 2009, in IAU Symposium, Vol. 256, IAU Symposium, Van Loon J. T., Oliveira J. M., eds., pp. 51–56
Mathewson D. S., Cleary M. N., Murray J. D., 1974, ApJ, 190, 291
McConnachie A. W., 2012, AJ, 144, 4
McMahon R., 2012, in Science from the Next Generation Imaging and Spectroscopic Surveys
Meschin I., Gallart C., Aparicio A., Hidalgo S. L., Monelli M., Stetson P. B., Carrera R., 2014, MNRAS, 438, 1067
Minniti D., Borissova J., Rejkuba M., Alves D. R., Cook K. H., Freeman K. C., 2003, Science, 301, 1508
Miyamoto M., Nagai R., 1975, PASJ, 27, 533
Mohr J. J. et al., 2012, in Society of Photo-Optical Instrumentation Engineers (SPIE) Conference Series, Vol. 8451, Society of Photo-Optical Instrumentation Engineers (SPIE) Conference Series
Moore B., Ghigna S., Governato F., Lake G., Quinn T., Stadel J., Tozzi P., 1999, ApJ, 524, L19
Navarro J. F., Frenk C. S., White S. D. M., 1996, ApJ, 462, 563
Nikolaev S., Drake A. J., Keller S. C., Cook K. H., Dalal N., Griest K., Welch D. L., Kanbur S. M., 2004, ApJ, 601, 260
Olsen K., Salyk C., 2002, The Astronomical Journal, 124,

2045
Olsen K. A. G., Massey P., 2007, ApJ, 656, L61
Piatti A. E., Geisler D., 2013, AJ, 145, 17
Putman M. E. et al., 1998, Nature, 394, 752
Renaud F., Gieles M., 2013, MNRAS, 431, L83
Rockosi C. M. et al., 2002, AJ, 124, 349
Rossetto B. M. et al., 2011, AJ, 141, 185
Rubele S. et al., 2012, A&A, 537, A106
Saha A. et al., 2010, AJ, 140, 1719
Schlegel D. J., Finkbeiner D. P., Davis M., 1998, ApJ, 500, 525
Sevilla I. et al., 2011, The Dark Energy Survey Data Management System
Skrutskie M. F. et al., 2006, AJ, 131, 1163
Soumagnac M. T. et al., 2013, Star/galaxy separation at faint magnitudes: Application to a simulated Dark Energy Survey
Staveley-Smith L., Kim S., Calabretta M. R., Haynes R. F., Kesteven M. J., 2003, MNRAS, 339, 87
Stetson P. B., 1987, PASP, 99, 191
Stewart K. R., Bullock J. S., Wechsler R. H., Maller A. H., Zentner A. R., 2008, ApJ, 683, 597
Subramaniam A., Subramanian S., 2009, ApJ, 703, L37
Swanson M., Tegmark M., Hamilton A., Hill C., 2012, Mangle: Angular Mask Software. Astrophysics Source Code Library
Swanson M. E. C., Tegmark M., Hamilton A. J. S., Hill J. C., 2008, MNRAS, 387, 1391
Tucker D. L. et al., 2007, in Astronomical Society of the Pacific Conference Series, Vol. 364, The Future of Photometric, Spectrophotometric and Polarimetric Standardization, Sterken C., ed., p. 187
van der Marel R. P., Cioni M.-R. L., 2001, AJ, 122, 1807
van der Marel R. P., Kallivayalil N., 2014, ApJ, 781, 121
van der Marel R. P., Kallivayalil N., Besla G., 2009, in IAU Symposium, Vol. 256, IAU Symposium, Van Loon J. T., Oliveira J. M., eds., pp. 81–92
Weinberg M. D., Nikolaev S., 2001, ApJ, 548, 712
Yang C.-C., Gruendl R. A., Chu Y.-H., Mac Low M.-M., Fukui Y., 2007, ApJ, 671, 374
Zacharias N., Finch C. T., Girard T. M., Henden A., Bartlett J. L., Monet D. G., Zacharias M. I., 2013, AJ, 145, 44

AFFILIATION

[1]Department of Physics, University of Surrey, Guildford GU2 7XH, UK
[2]Departamento de Astronomia, Universidade Federal do Rio Grande do Sul, Av. Bento Gonçalves 9500, Porto Alegre 91501-970, RS, Brazil
[3]Laboratório Interinstitucional de e-Astronomia - LIneA, Rua Gal. José Cristino 77, Rio de Janeiro, RJ - 20921-400, Brazil
[4]Osservatorio Astronomico di Padova INAF, Vicolo dell'Osservatorio 5, I-35122 Padova, Italy
[5]Observatório Nacional, Rua Gal. José Cristino 77, Rio de Janeiro, RJ - 20921-400, Brazil
[6]Astronomy Department, University of Illinois, 1002 W. Green St., Urbana, IL 61801, USA
[7]National Center for Supercomputing Applications, University of Illinois, 1205 W Clark St., Urbana, IL 61801, USA
[8]Cerro Tololo Inter-American Observatory, National Optical Astronomy Observatory, Casilla 603, La Serena, Chile
[9]Fermi National Accelerator Laboratory, P.O. Box 500, Batavia, IL 60510 USA
[10]Department of Physics & Astronomy, University College London, Gower Street, London WC1E 6BT, UK
[11]Space Telescope Science Institute (STScI), 3700 San Martin Drive, Baltimore, MD 21218
[12]Argonne National Laboratory, 9700 South Cass Avenue, Lemont, IL 60439, USA
[13]Carnegie Observatories, 813 Santa Barbara St., Pasadena, CA 91101, USA
[14]Institut d'Astrophysique de Paris, Univ. Pierre et Marie Curie & CNRS UMR7095, F-75014 Paris, France
[15]Kavli Institute for Particle Astrophysics and Cosmology 452 Lomita Mall, Stanford University, Stanford, CA, 94305
[16]George P. and Cynthia Woods Mitchell Institute for Fundamental Physics and Astronomy, and Department of Physics and Astronomy, Texas A&M University, College Station, TX 77843, USA
[17]Department of Physics, Ludwig-Maximilians-Universität, Scheinerstr. 1, 81679 München, Germany
[18]Excellence Cluster Universe, Boltzmannstr. 2, 85748 Garching, Germany
[19]Department of Physics, University of Michigan, Ann Arbor, MI 48109, USA
[20]Department of Astronomy, University of Michigan, Ann Arbor, MI 48109, USA
[21]Max Planck Institute for Extraterrestrial Physics, Giessenbachstrasse, 85748 Garching, Germany
[22]Department of Physics, The Ohio State University, Columbus, OH 43210, USA
[23]Australian Astronomical Observatory, North Ryde, NSW 2113, Australia
[24]Department of Physics and Astronomy, Center for Particle Cosmology, University of Pennsylvania, 209 South 33rd Street, Philadelphia, PA 19104, USA
[25]Institut de Física d'Altes Energies, Universitat Autònoma de Barcelona, E-08193 Bellaterra (Barcelona), Spain
[26] Institució Catalana de Recerca i Estudis Avançats, E-08010 Barcelona, Spain
[27]Brookhaven National Laboratory, Bldg 510, Upton, NY 11973, USA
[28]Centro de Investigaciones Energéticas, Medioambientales y Tecnológicas (CIEMAT), Av. Complutense 40, 28040 Madrid, Spain
[29]SLAC National Accelerator Laboratory, Menlo Park, CA 94025, USA
[30]Jodrell Bank Centre for Astrophysics, University of Manchester, Alan Turing Building, Manchester, M13 9PL, U.K.